

Supporting Information

Boosted microwave absorption performance of multi-dimensional Fe₂O₃/CNTsCM@CN assembly by enhanced dielectric relaxation

Xuefeng Yu,^{‡a} Ying Zhang,^{‡a} Lei Wang,^a Linshen Xing,^a Wenbin You,^a Jiwei Liu,^b Guanyu Chen,^a Guangzhou Ding,^a Jingjun Ding,^a Xianhu Liu,^c Min Wang,^{*a} Renchao Che^{*a}

[‡] The authors have contributed equally to this work

^aLaboratory of Advanced Materials, Department of Materials Science and Collaborative Innovation Center of Chemistry for Energy Materials (iChem), Fudan University, Shanghai 200438, P.R. China

^bSchool of Materials Science and Engineering, Changzhou University, Changzhou, Jiangsu 213164, People's Republic of China

^cKey Laboratory of Materials Processing and Mold (Zhengzhou University), Ministry of Education, Zhengzhou 450002, China

* E-mail: rcche@fudan.edu.cn

* E-mail: minwang@fudan.edu.cn

Figures

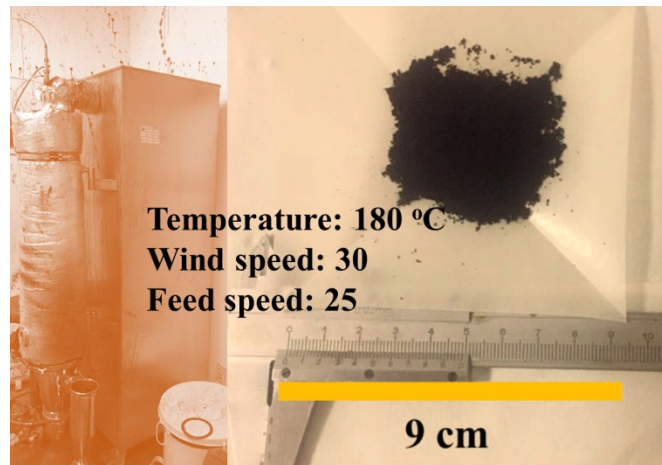


Fig S1. The digital photograph of spray-dried equipment and the corresponding synthesized products. Notably, the fabricated samples are large scale and cost-efficient for further application.

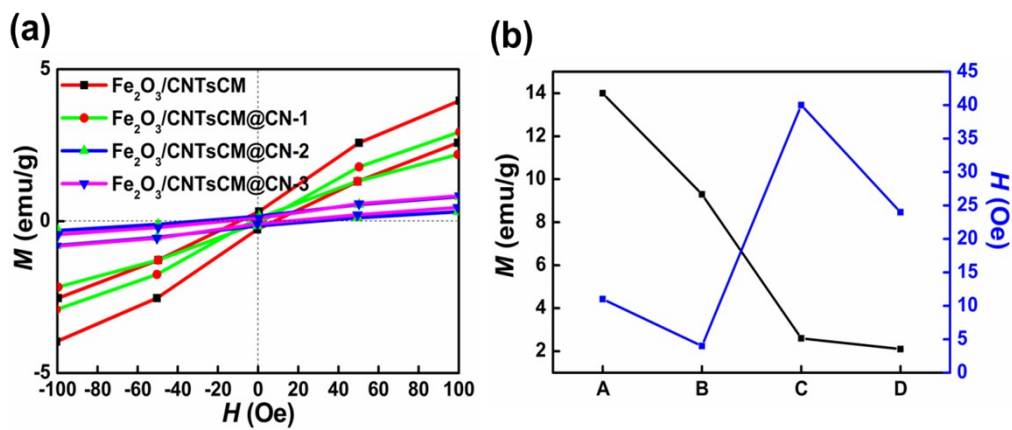


Fig S2. (a) The enlargement magnetic hysteresis loops from -100 Oe to 100 Oe and (b) the resulted magnetic parameters of as-fabricated samples: A $\text{Fe}_2\text{O}_3/\text{CNTsCM}$, B $\text{Fe}_2\text{O}_3/\text{CNTsCM@CN-1}$, C $\text{Fe}_2\text{O}_3/\text{CNTsCM@CN-2}$, and D $\text{Fe}_2\text{O}_3/\text{CNTsCM@CN-3}$.

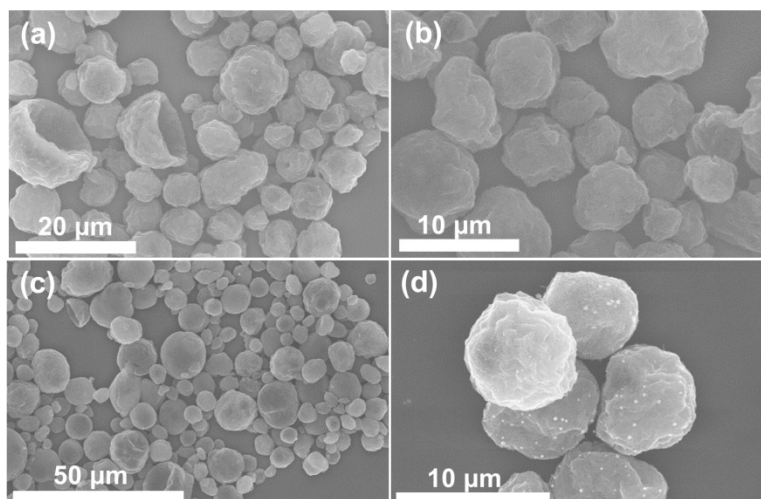


Fig S3. (a)-(b) The FFSEM image of Fe₂O₃/CNTsCM; (c)-(d) The FFSEM image of Fe₂O₃/CNTsCM@CN-1.

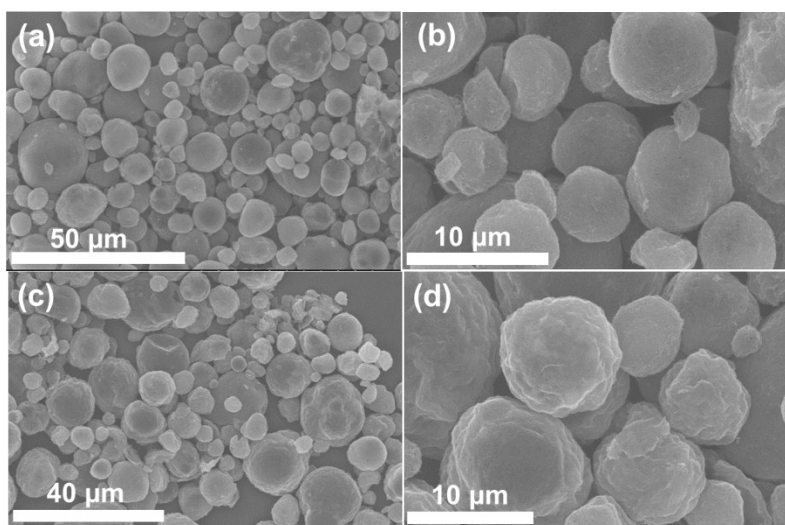


Fig S4. (a)-(b) The FFSEM image of Fe₂O₃/CNTsCM@-2; (c)-(d) The FFSEM image of Fe₂O₃/CNTsCM@CN-3.

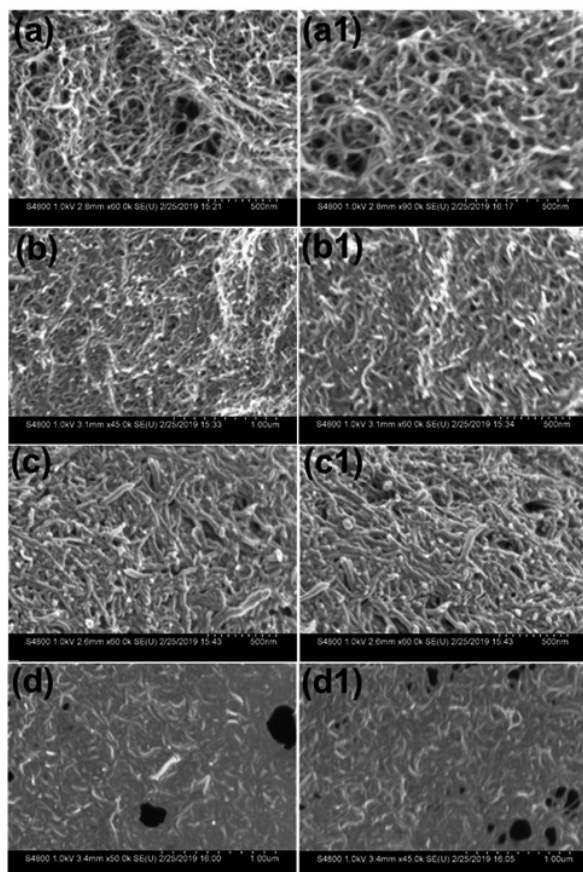


Fig S5. The SEM images of the detailed surface of (a-a1) $\text{Fe}_2\text{O}_3/\text{CNTsCM}$, (b-b1) $\text{Fe}_2\text{O}_3/\text{CNTsCM}@CN-1$, (c-c1) $\text{Fe}_2\text{O}_3/\text{CNTsCM}@CN-2$, and (d-d1) $\text{Fe}_2\text{O}_3/\text{CNTsCM}@CN-3$.

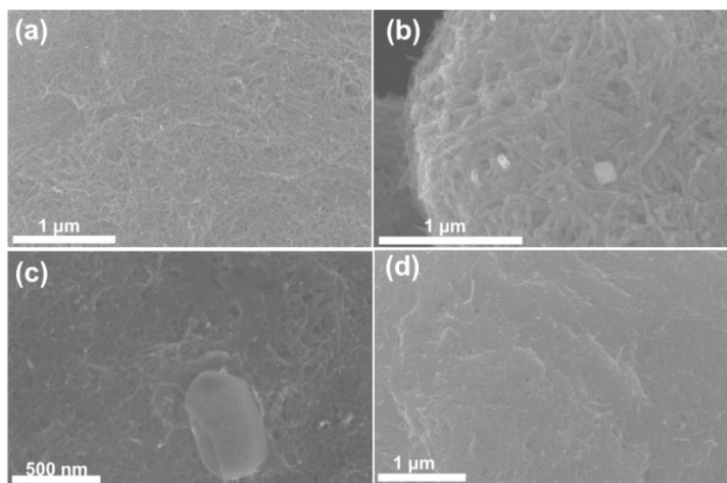


Fig S6. The FFSEM images of the detailed surface of (a) $\text{Fe}_2\text{O}_3/\text{CNTsCM}$, (b) $\text{Fe}_2\text{O}_3/\text{CNTsCM}@CN-1$, (c) $\text{Fe}_2\text{O}_3/\text{CNTsCM}@CN-2$, (d) $\text{Fe}_2\text{O}_3/\text{CNTsCM}@CN-3$.

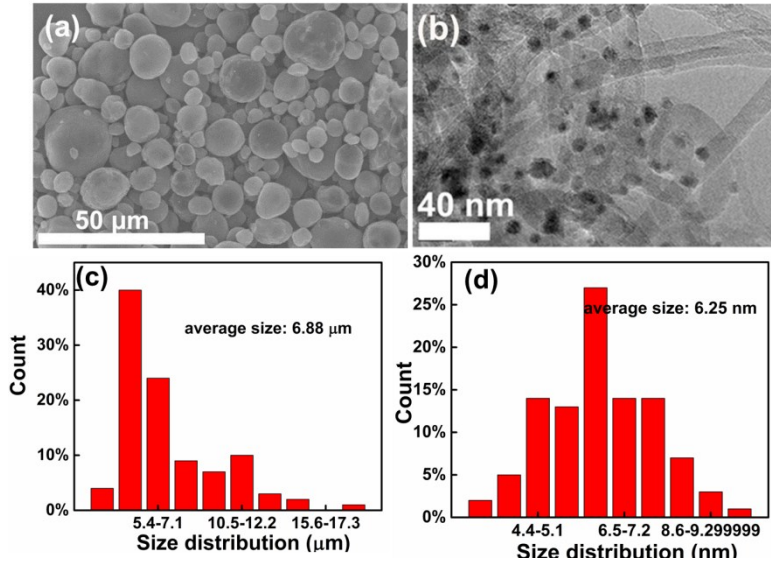


Fig S7. The SEM image (a) and TEM image (b) of $\text{Fe}_2\text{O}_3/\text{CNTsCM}@CN-2$. The corresponding size distribution (c)-(d) of $\text{Fe}_2\text{O}_3/\text{CNTsCM}@CN-2$ sample.

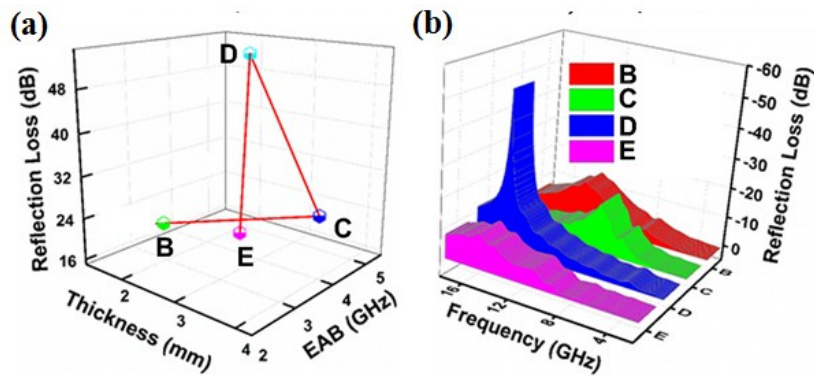


Fig S8. (a) The comprehensive comparison of the microwave absorption properties of as-prepared samples in the frequency range of 2–18 GHz. (b) The comparison of the maximum $|RL|$ of hybrid composites at the same thickness of 2 mm. B $\text{Fe}_2\text{O}_3/\text{CNTsCM}$; C $\text{Fe}_2\text{O}_3/\text{CNTsCM}@CN-1$; D $\text{Fe}_2\text{O}_3/\text{CNTsCM}@CN-2$; E $\text{Fe}_2\text{O}_3/\text{CNTsCM}@CN-3$.

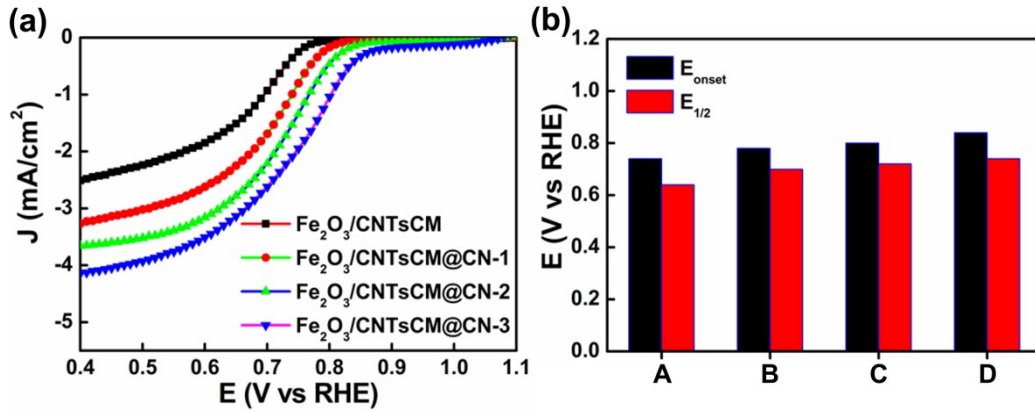


Fig S9. (a) The LSV curves of as-synthesized samples (ORR measurement); the ORR performance comparison among these samples: A $\text{Fe}_2\text{O}_3/\text{CNTsCM}$, B $\text{Fe}_2\text{O}_3/\text{CNTsCM}@-1$; C $\text{Fe}_2\text{O}_3/\text{CNTsCM}@-2$; D $\text{Fe}_2\text{O}_3/\text{CNTsCM}@-3$.

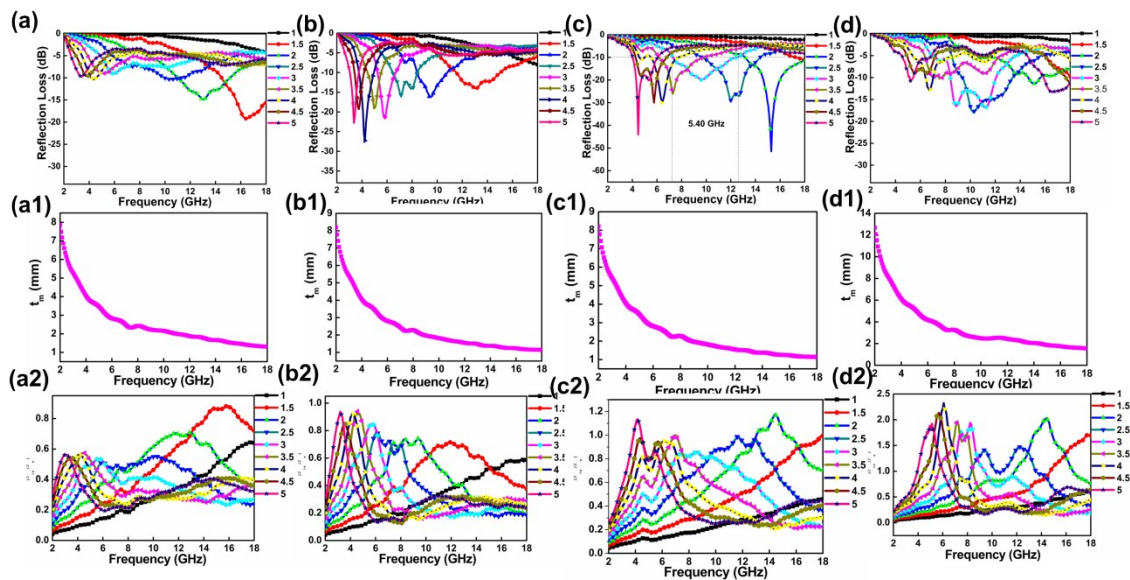


Fig S10. The reflection loss values of as-prepared composites with different thicknesses. (a) $\text{Fe}_2\text{O}_3/\text{CNTsCM}$, (b) $\text{Fe}_2\text{O}_3/\text{CNTsCM}@-1$, (c) $\text{Fe}_2\text{O}_3/\text{CNTsCM}@-2$, (d) $\text{Fe}_2\text{O}_3/\text{CNTsCM}@-3$; the $1/4 \lambda$ values of as-prepared composites that are related to the scattering and reflection loss: (a1) $\text{Fe}_2\text{O}_3/\text{CNTsCM}$, (b1) $\text{Fe}_2\text{O}_3/\text{CNTsCM}@-1$, (c1) $\text{Fe}_2\text{O}_3/\text{CNTsCM}@-2$, (d1) $\text{Fe}_2\text{O}_3/\text{CNTsCM}@-3$; the calculated impedance matching value ($Z=Z_{in}/Z_0$) of composites in the frequency range of 2-18 GHz. (a2) $\text{Fe}_2\text{O}_3/\text{CNTsCM}$, (b2) $\text{Fe}_2\text{O}_3/\text{CNTsCM}@-1$, (c2) $\text{Fe}_2\text{O}_3/\text{CNTsCM}@-2$, (d2) $\text{Fe}_2\text{O}_3/\text{CNTsCM}@-3$.

As is shown by Fig. S10a1-d1, the interrelationships between matching thickness (t_m) and matching frequency (f_m) can be illustrated by the $1/4$ wavelength cancellation theories:

$$t_m = n\lambda/4 = \frac{nc}{4f_m\sqrt{|\mu_r||\epsilon_r|}} \quad (n=1, 3, 5 \dots)$$

In which f_m is the electromagnetic frequency, t_m is the matching thickness, c is the light velocity. Strikingly, benefited from the hierarchical assembly fabricated by the 0D γ - Fe_2O_3 nanoparticles, 1D carbon nanotubes (CNTs) and 2D N-doped carbon layer, the abundant reflection or scattering sites can be introduced to these composite systems. Considering the matching thickness satisfying with the 1/4 wavelength cancellation equation, the incident microwave can be reflected or scattered from these sites with opposite phases of 180° , thereby improving the electromagnetic energy dissipation. To sum up, induced by the unique structure-performance effect, the reflection loss and scattering loss of the micron-scale composite materials can be largely strengthened, which is more beneficial for the total microwave absorption.

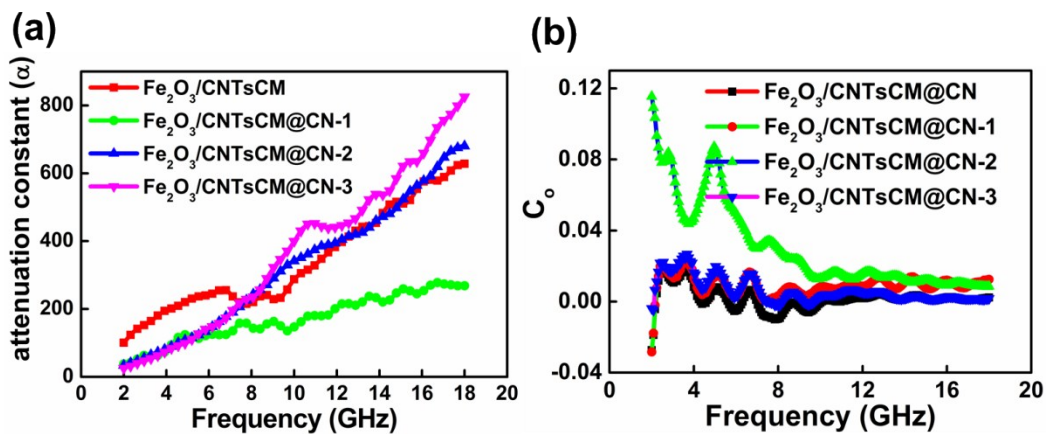


Fig S11. (a) The C_o values, (b) the attenuation constant factor α of these as-synthesized samples in the frequency range of 2-18 GHz.

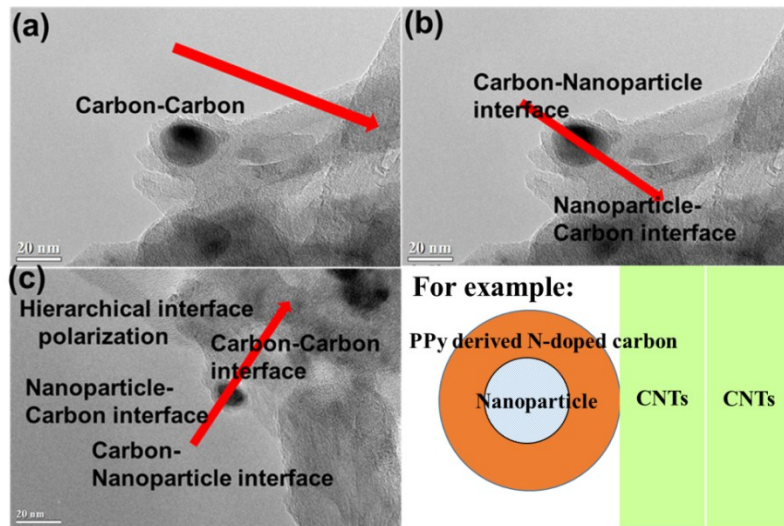


Fig S12. The TEM picture of hierarchical polarized heterojunction interfaces marked by red arrow. (a) Carbon-carbon interface (b) Carbon-nanoparticles-carbon-carbon interfaces (c) hierarchical heterojunction interfaces (d) The schematics diagram for hierarchical polarized heterojunction interfaces.

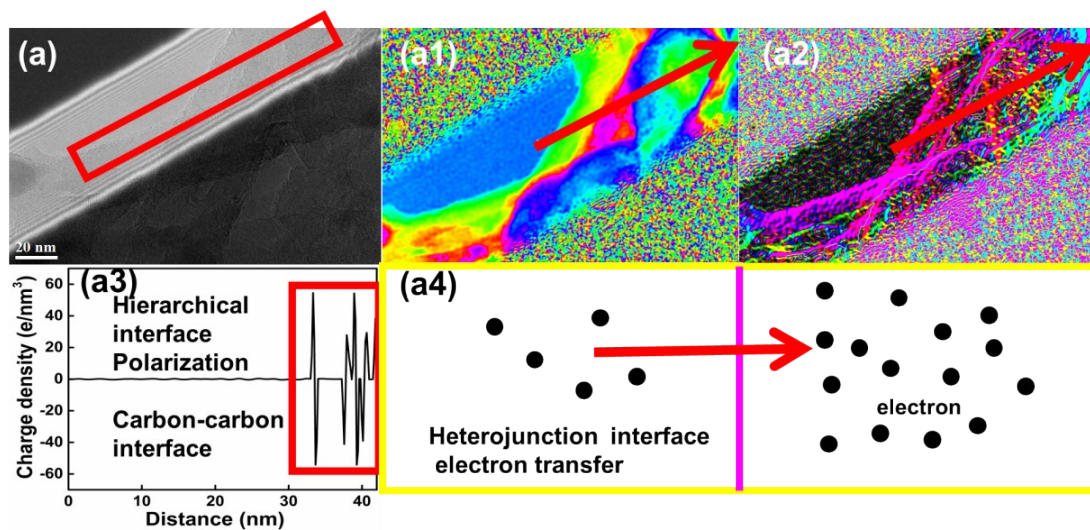


Fig S13. As exemplified by $\text{Fe}_2\text{O}_3/\text{CNTsCM@CN-2}$, (a) Off-axis electron holograms; (a1) reconstructed phase image; (a2) electric field distribution picture (The different color variations indicate the direction of the built-in electric field, and the intensity of the same type color indicates the intensity of the built-in electric field); (a3) the corresponding profile lines of charge density. (a4) The schematics diagram for the electron transfer along with the polarization heterojunction interface. Clearly, a lot of interface polarization relaxation can be introduced benefiting from the unique structure assembly.

To clarify interfacial polarization effect, the related charge density distribution of $\text{Fe}_2\text{O}_3/\text{CNTsCM@CN-2}$ composite was revealed by off-axis

electron holography (Fig. S13). Implementing with the follow-up treatment of hologram images (Fig. S13a), the corresponding electrostatic potential information can be further analyzed in view of the Poisson's equation (Fig. S13a1). Exemplified by CNTs-CNTs interfaces in Fig. S13a3, the strong charge transfer behaviors along with the heterojunction interfaces can happen on, resulting in the charge redistribution. For as-synthesized $\text{Fe}_2\text{O}_3/\text{CNTsCM@CN}$ composites, attributed to the forcibly-assembled strategy the abundant heterojunction interfaces, among 2D N-doped carbon, 0D $\gamma\text{-Fe}_2\text{O}_3$ and 1D CNTs, can be generated. These tight contacting can mainly include CNTs-CNTs interface, CNTs-nanoparticles interface, N-doped carbon layers-CNTs interface, N-doped carbon layers-nanoparticles interface, and N-doped carbon layers-nanoparticles-N-doped carbon layers-CNTs-CNTs interface and so on. As a result, a great deal of built-in electric field in these hybrid systems has been constructed, ultimately boosting interfacial polarization effect.

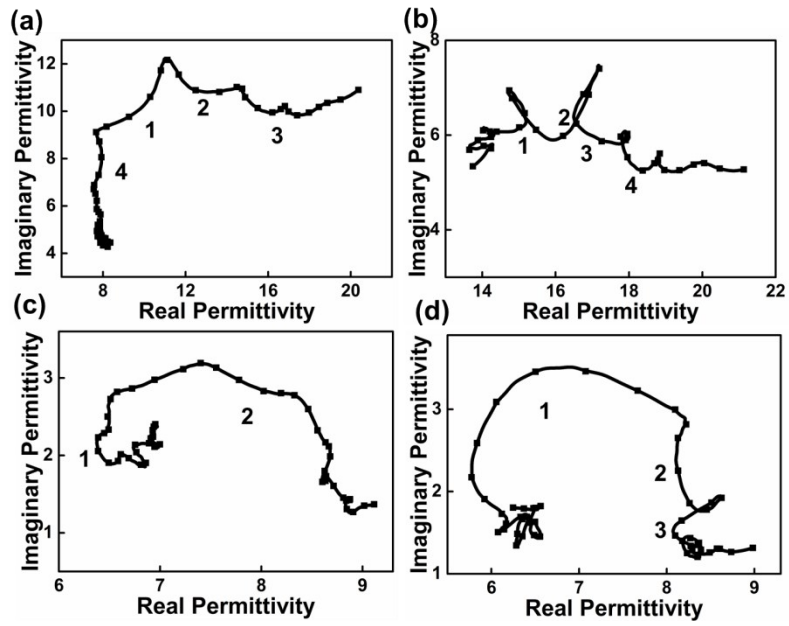


Fig S14. The typical Cole-Cole semicircles of as-fabricated composite samples in 2-18 GHz: (a) $\text{Fe}_2\text{O}_3/\text{CNTsCM}$; (b) $\text{Fe}_2\text{O}_3/\text{CNTsCM}@-1$; (c) $\text{Fe}_2\text{O}_3/\text{CNTsCM}@-2$; (d) $\text{Fe}_2\text{O}_3/\text{CNTsCM}@-3$.

Table S1. The compared microwave absorption performances of as-synthesized samples and other carbon-based nanomaterials.

Absorber	Synthetic method	Mass ratio (wt %)	Measured thickness (mm)	RL _{min} Values (dB)	absorption band (GHz) (RL < -10 dB) from 1.00 to 5.00 mm	refs
monodisperse Fe ₃ O ₄ /C nanosheets	carbothermal reduction preparation	—	4.3 mm	-43.95 dB	12.7 GHz	22
composite graphene aerogel	surface and interface reinforce approach	15 %	4.0 mm	-49 dB	13.6 GHz	43
Fe/Fe ₃ C@NCNTs- 600	direct pyrolysis method	30 %	4.97 mm	-46.0 dB	14.8 GHz	44
porous Fe ₃ O ₄ / carbon fiber	graphitization Process of bagasse waste	30 %	1.9 mm	-48.2 dB	13.8 GHz	45
Fe ₃ O ₄ /graphene capsules	catalytic chemical vapor deposition (CCVD) and hydrothermal process	30 %	3.5 mm	-32 dB	11.6 GHz	46
FeCo alloy/carbon composites	in situ pyrolysis of Prussian blue analogues	40 %	2 mm	-33 dB	14.8 GHz	47
Graphene/Fe ₃ O ₄ aerogel microspheres	electrospinning-freeze drying	5 %	4.0 mm	-51.5 dB	—	48
3D porous carbon/Fe ₃ O ₄ @Fe composites	carbonization process of loofah sponge	30 %	2 mm	-49.6 dB	—	49
ACHFs-CNTs-Fe ₃ O ₄	chemical vapor deposition	28 %	2.5 mm	-46.828 dB	13.54 GHz	50
PVDF/Fe ₃ O ₄ @PPy	electrospinning	—	2.5 mm	-21.5 dB	13.2 GHz	51
biomass-derived porous carbon materials foam	sol-gel and carbonization process	30 %	4.7 mm	-43.6 dB	—	52
carbon cloth substrate@ZnO	in situ orientation growth process	40%	3.5 mm	-43.7 dB	10.04 GHz	53
Fe ₂ O ₃ /CNTs@CN-2	Spray-drying method	10 %	2.0 mm	-51.5 dB	14.01 GHz	herein